Chapter 12
Investigations on the Influence of Strain Rate, Temperature and Reinforcement on Strength and Deformation Behavior of CrMnNi-Steels

Ralf Eckner, Christine Baumgart, and Lutz Krüger

Abstract This section presents the results of comprehensive investigations into the strength and deformation behavior of CrMnNi-TRIP/TWIP steels and particle-reinforced TRIP-Matrix-Composites. These investigations combined quasi-static and dynamic tensile, compressive, and plate impact tests with ex situ microstructure analysis using electron microscopy and diffraction techniques on representative samples. The aim was the investigation and microstructurally-based description and modeling of the temperature and strain rate dependent strength, deformation and failure behavior of these advanced materials. It could be shown that the behavior of austenitic CrMnNi steels is controlled by different deformation mechanisms. These include mechanical twinning and martensitic phase transformations, whose occurrences or interactions are influenced by the chemical composition or the austenite stability, the stacking fault energy, the deformation temperature and rate as well as by the loading direction. Furthermore, the mechanical properties of honeycomb structures made of CrMnNi steel or TRIP-Matrix-Composites have been investigated. These are intended as lightweight and high strength components to improve the crash performance of constructions in the field of mobility. Since their mechanical properties are influenced by several parameters such as the chemical composition of the material, the structure type or the reinforcement content, detailed analyses are necessary before their application in vehicle components.

R. Eckner (Emeritus)
Institute of Materials Engineering, Technische Universität Bergakademie Freiberg, Gustav-Zeuner-Str. 5, 09599 Freiberg, Germany

C. Baumgart · L. Krüger (✉)
Institute of Materials Engineering, Technische Universität Bergakademie Freiberg, Gustav-Zeuner-Str. 5, 09599 Freiberg, Germany
e-mail: krueger@ww.tu-freiberg.de

H. Biermann and C. G. Aneziris (eds.), *Austenitic TRIP/TWIP Steels and Steel-Zirconia Composites*, Springer Series in Materials Science 298,
https://doi.org/10.1007/978-3-030-42603-3_12

12.1 Introduction

The automotive industry is always looking for ways to increase safety and performance while reducing fuel consumption. These requirements led to the development of so-called *High Strength Steels* (HSS) and *Advanced High Strength Steels* (AHSS). Among these, high-alloy austenitic stainless steels are characterized by extraordinary properties such as excellent formability, high corrosion resistance, and good weldability, and are used for applications ranging from cryogenic up to elevated temperatures. Such steels take advantage of the TRIP- and/or TWIP-effects (TRansformation Induced Plasticity or TWinning Induced Plasticity), which are both triggered by plastic deformation and depend strongly on the stacking fault energy of the steel. At relatively high stacking fault energies (>40 mJ/m^2), the material deforms and hardens substantially due to the motion of dislocations. Stacking fault energies between 20 and 40 mJ/m^2 favor the emergence of stacking faults and deformation twins (TWIP-effect) [1–3]. Such planar defects act as obstacles for further dislocation movement and consequently increase the strain hardening rate of the material, which is known as the "dynamic Hall-Petch effect" [4]. In steel with lower stacking fault energy, the TRIP-effect is evident which is associated with the formation of ε- and α'-martensite and involves the enhancement of strength and ductility below the M_d-temperature [5–7]. The stacking fault energy mainly depends on the chemical composition of the steel and the deformation temperature [8]. The necessary mechanical driving force for the transformation $\gamma \rightarrow \alpha'$ is provided by the mechanical stress applied on the material [7]. Both mechanisms are already being used in the development of modern advanced high strength steels, e.g. for automotive applications [9]. These materials offer great potential for improving occupant safety in the event of a crash as well as for lightweight construction to reduce weight and energy consumption.

Within the Collaborative Research Center 799, two development routes are utilized in order to generate weight efficient energy absorbing materials. On the one hand, the combination of two different material groups. This exploits the beneficial properties of each component, like in the case of mother-of-pearl, and is implemented by reinforcing ductile TRIP-steel with high strength MgO partially stabilized zirconia (Mg-PSZ) [10]. On the other hand, the use of these metal matrix composites (MMC) in cellular networks follows the example of wood or cork which could have a favorable strength to weight ratio [11]. Those cellular materials belong to the honeycomb-like structures. Unlike established materials for cellular structures such as aluminum, titanium or magnesium, TRIP-steel and TRIP-Matrix-Composites do not belong to light metals. However, it has been proven that the deformation induced phase transformation of TRIP-steels is an energy consuming process which helps to balance the influence of a higher density when comparing the specific energy absorption capability of different structures [12].

The intention of the present survey is to highlight the deformation mechanisms which are active under dynamic loading and under shock wave loading by flyer-plate impact in bulk cast high-alloy CrMnNi TRIP/TWIP-steel. Detailed investigations of the developed microstructure were performed in order to explain the experimental results, with special focus on the martensitic transformation. Furthermore, static

compression tests were conducted at room temperature in order to compare the fundamental performance of the different cellular materials made of TRIP-steel and TRIP-Matrix-Composites with focus on the compressive strength, deformation and damage behavior.

12.2 High Strain Rate Deformation of Austenitic High-Alloy TRIP/TWIP Steel

12.2.1 Processing and Experimental Methods

Table 12.1 represents the chemical compositions of the investigated high-alloy austenitic TRIP/TWIP steel. The examined material is based on a patent-protected development [13] and is described as 16-6-6, according to the concentrations of Cr, Mn, and Ni in wt%. The material was cast in plates (dimensions 200 × 200 × 16 mm^3) by ACTech GmbH (Freiberg, Germany) using sand casting technology. The manufactured samples were subsequently solution-heat-treated at 1323 K (1050 °C) for 30 min to retransform any martensite induced by previous machining. A dendritic austenite microstructure with coarse grains in the range of 100–1000 μm was received. Due to the chemical composition of the steel, a certain amount of δ-ferrite (~2 vol%) was formed during solidification. This steel belongs to AHSS of the 1st generation and is characterized by a high strain hardening capacity in combination with high formability, though the yield strength is rather low (YS ~200 MPa, UTS ~800 MPa, total elongation ~50%) [14].

Quasistatic compression tests at 0.0004 1/s were performed in a servohydraulic universal testing machine. For the dynamic impact and high-rate experiments up to 2300 1/s a drop weight tower and a Split-Hopkinson pressure bar system (SHPB) were used [15]. All mechanical tests were carried out on cylindrical samples with 6 mm in diameter and 6 mm in height. The samples were instrumented with strain gauges in order to allow a local deformation measurement even at high deformation speeds. In order to obtain consistent high rate compressive stress/strain data, the SHPB apparatus was modified by a pulse shaping technique using OFHC-copper platelets [16] and numerical dispersion correction [17].

In order to determine the strength properties of the test material, a flyer-plate impact assembly of the Russian Academy of Sciences, Institute of Problems of Chemical Physics, Chernogolovka near Moscow was used, which is shown schematically in Fig. 12.1. The test specimens had a thickness of 5 mm with a square area of 45 ×

Table 12.1 Chemical composition of the investigated high-alloy CrMnNi TRIP/TWIP steel

(wt%)	C	N	Cr	Mn	Ni	Si	Fe + others
Cast X3CrMnNi16-6-6 (abbr.: 16-6-6)	0.03	0.03	15.5	6.1	6.1	0.9	Bal.

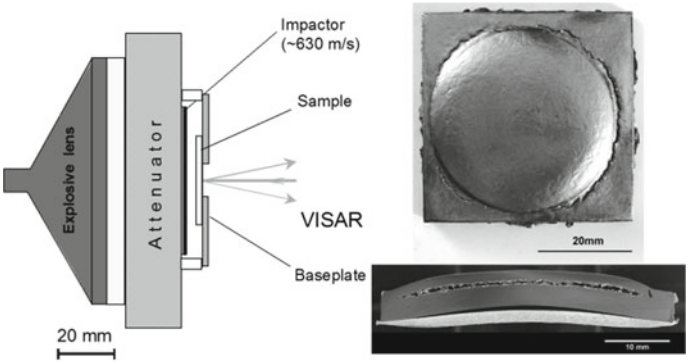

Fig. 12.1 Schematic setup of the plate impact experiments to determine the strength properties under planar shock loading at room temperature [20]

45 mm^2 and were shocked by plates (thickness 2 mm) of technically pure aluminum. The acceleration of the flyer-plates was carried out by means of a blasting lens to speeds of 650 ± 30 m/s. The shock pressure yielded 7–8 GPa and the strain rate behind the wave front and before spallation was 5–6 × 10^4 1/s. The planar impact of the aluminum plate produced a shock wave within the target sample and resulted in a uniaxial state of deformation over a pulse length of less than one microsecond. Therefore, the free surface velocity profiles were recorded using VISAR Laser Doppler Velocimetry [18] with a time resolution of ~1 ns and a space resolution of ~0.1 mm^2, giving a measurement accuracy of ~5 m/s. Evaluation of such plate-impact experiments is described in detail for instance in [19].

For shock wave experiments on large-volume samples at higher pressures, a plate-impact setup of the Freiberg High Pressure Research Center (FHP) was also used, which is shown schematically in Fig. 12.2. This experimental setup was originally developed for the high-pressure synthesis of ultra-hard materials (Diamond, c-BN, γ-Si_3N_4) and builds up on the findings and specifications of the EMI (Ernst Mach-Institute) in Freiburg [21]. The difference to the above-described plate impact structure of the Russian Academy of Sciences consists in the ability to produce reproducible pressures up to 120 GPa or more within the sample and thereby have a much larger sample volume available.

In the experiments, the amount of explosive used was varied, whereby pressures of 30, 60, 90 and 120 GPa (or 0.3–1.2 Mbar) could be set. After ignition, the flyer-plate was accelerated over a distance of 20 mm and then hit flat on the sample surface. Depending on the amount of explosive, the final velocity varied between 1.5 and 4 km/s. The target, the cylindrical material sample, was located in a form-fitting round container with a diameter of 220 mm, which was made of structural steel S355 (St-52). Below the sample a hardened steel plate was positioned, which was supported on a sand bed and acted as a damping plate or impulse trap. This design pursued two goals; on the one hand, the sample container prevented the free adiabatic expansion of the sample. On the other hand, the impedance difference between the

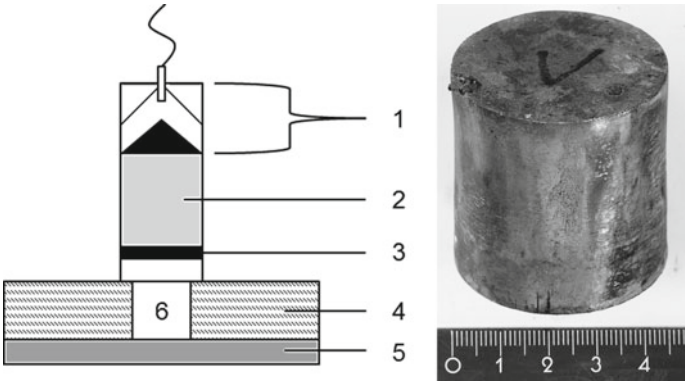

Fig. 12.2 Setup for shock experiments on large-volume samples: (1) plane wave generator with electric detonator (PETN explosive) (2) C-4 explosive (3) CrMnNi steel flyer-plate, (4) structural steel container (S355), (5) QT steel plate, (6) CrMnNi steel sample [22]

sample and the overlay was small, so that the shockwave was not reflected at the interface and the spallation could be prevented. Thus, the sample remained intact during the experiment and could then be mechanically removed from the sample container.

After mechanical testing, the α'-martensite volume fraction was quantified using a Metis MSAT type magnetic saturation device for both, the deformed compression specimens and shock-loaded conditions. For light-optical characterization, the samples were ground, polished, and etched with Beraha II etchant or V2A etchant, in order to contrast the deformation features such as deformation bands or martensite. Subsequently, microstructural investigations were carried out by scanning electron microscopy (SEM), transmission electron microscopy (TEM) in combination with electron backscatter diffraction (EBSD), selected area electron diffraction (SAED) or convergent beam electron diffraction (CBED) techniques.

12.2.2 Approaches to Rate-Dependent Constitutive Modeling

The influence of strain rate on the flow curves and the hardening behavior of metastable austenitic CrMnNi steels is of great importance considering technical application fields. Their plastic deformation is based essentially on the separation of Shockley partial dislocations and the subsequent stacking fault and deformation band formation [23, 24]. The increasing stacking fault density as well as the development of ε- and α'-martensite nuclei leads in consequence to strain hardening or to the dynamic Hall-Petch effect. However, the adiabatic sample heating effect increases with increasing strain rate, whereby much of the plastic deformation work remains in the sample as thermal energy. A nonlinear development of strain and strength characteristics with increasing strain rate is usually caused by this phenomenon. It

was as well shown that the α'-martensite formation rate decreases with increasing strain rate and tends towards zero at high strain values ($\varepsilon \geq 0.3$) [25], caused by an increasing stacking fault energy and a reduction in chemical driving force for the $\gamma \rightarrow \alpha'$ transformation [26, 27]. Previous studies highlighted the influence of a temperature change on the SFE and the separation distance of dislocations in detail [28]. The splitting into partial dislocations and the corresponding stacking fault formation require a critical stress level, which increases with increasing SFE. The SFE in turn increases with increasing temperature. In addition, both an increase in temperature and an increased strain rate increase the threshold stress for martensite formation [28, 29]. However, this effect is partly compensated, since the threshold stress for stacking fault or twin formation can be achieved at even lower strain values due to the rise in yield strength with increasing strain rate [30].

The reduced rate of martensite formation and the consequent decreasing strain hardening with increasing strain rate cause a decrease in flow stress with increasing deformation [25, 31]. On this occasion, the so-called curve crossing phenomenon can occur, whereby the strain softening leads to the intersection of the dynamic flow curves with the quasi-static flow curves [32]. In general, flattening of the flow curves can be observed at high strain rates, which is associated with a reduced maximum strength. The characteristic strain hardening curve is shifted to lower values and lower deformations, and the sigmoidal character changes into a plateau or disappears [33–35]. Furthermore, sample heating in high-speed tests leads to a decrease in the volume fraction of austenite converted into α'-martensite [25, 27, 36, 37]. Depending on the alloy composition and the degree of sample heating, a change in the dominant deformation mechanism is also possible, from stacking fault/ε-martensite formation to twinning or dislocation glide [8]. This transition is associated with decreasing strain hardening capability during deformation. Figure 12.3 shows results of strain-rate-dependent compression tests on the 16-6-6 steel alloy as an example for the effects mentioned. As expected, increasing strain rate led to crossing of the flow curves (Fig. 12.3a) owing to reduced strain hardening due to a lower fraction of α'-martensite formed (Fig. 12.3b).

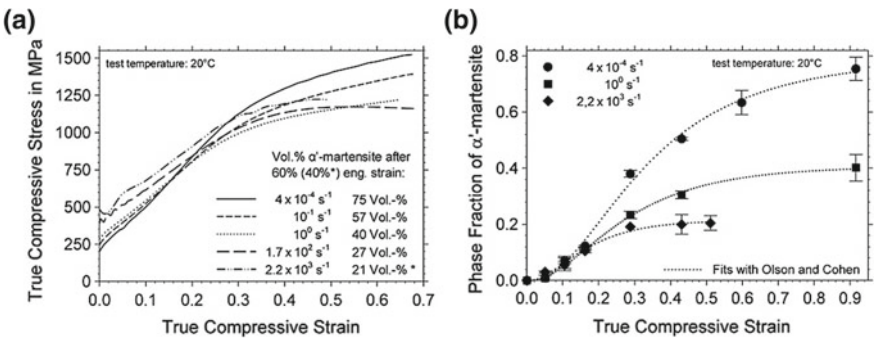

Fig. 12.3 CrMnNi16-6-6 steel: **a** Strain rate dependent mechanical behavior under compressive loading and **b** martensite kinetics at various strain rates (fitted according to [6]) [38]

Within the scope of the investigations, an empirical model of the flow stress on the basis of the rule of mixture (RM) was developed, which includes all important microstructural deformation mechanisms of CrMnNi TRIP steels as a function of temperature and strain rate. Several earlier research works dealt with the problem of modelling a deformation-induced martensitic transformation in austenitic steels. At this point, the publications of Ludwigson and Berger [39] and of Narutani et al. [40] are considered more in detail, representing two of the most significant works.

Ludwigson and Berger pointed out that the flow behavior of austenitic steel differs significantly from that of carbon steel due to the strain-induced martensitic transformation. For this reason, the flow curve cannot be described only by the relationship in (12.1),[1] which is valid for a variety of steels.

$$\sigma = K \cdot [\ln(1+\varepsilon)]^n \tag{12.1}$$

They assumed an autocatalytic formation reaction of the martensite and were therefore able to extend the existing model by a strength contribution of the martensitic phase depending on the actual strain value. Ludwigson and Berger introduced a factor A, which describes the ease with which an austenitic structure can undergo a strain-induced transformation to martensite, and the factors C and Q which characterize the martensite strength contribution. Equation (12.2)[2] shows the corresponding flow-curve equation relating true stress to strain.

$$\sigma = K[\ln(1+\varepsilon)]^n \cdot \left[1 - \left(1 + \frac{\varepsilon^{-B}}{A}\right)^{-1}\right] + C\left(1 + \frac{\varepsilon^{-B}}{A}\right)^{-Q} \tag{12.2}$$

Narutani et al. later recognized that for a more accurate description of the flow curves, it is also necessary to incorporate a softening term into the model. This necessity arises from the operation of the martensitic transformation as an additional deformation mechanism. For this reason, they developed a strain-corrected rule of mixture model (SCRM), based on the data of a metastable austenite, a stable austenite and a martensitic steel variant. Their complete constitutive relation for the plastic flow of metastable austenitic steel shows the following (12.3).[3]

---

[1] K = strength factor
n = strain-hardening index.

[2] A = factor describing the driving force for strain-induced $\gamma \rightarrow \alpha'$ transformation
B = factor describing the autocatalytic effect of transformed martensite
C = factor representing the flow stress of a fully martensitic structure
Q = factor describing stress contribution of the transformed martensite.

[3] $f_{\alpha'}$ = volume fraction of α'-martensite
α, β = material coefficients from the analysis of experimental data
σ_γ = flow stress of stable austenite
$\sigma_{\alpha'}$ = flow stress of martensite.

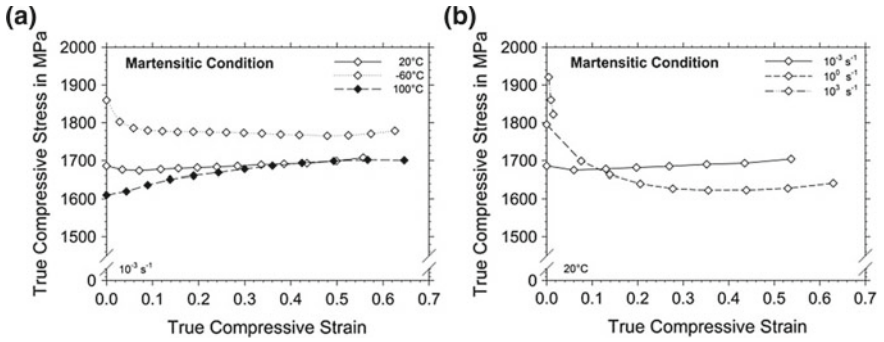

Fig. 12.4 CrMnNi16-6-6 steel: True stress-true strain curves of the α'-martensite phase: **a** influence of temperature and **b** strain rate effects [41]

$$\sigma = \left\{[1 - f_{\alpha'}] \cdot \sigma_{\gamma}(\varepsilon - \alpha \cdot f_{\alpha'}) + f_{\alpha'} \cdot \sigma_{\alpha'}(\varepsilon - \alpha \cdot f_{\alpha'})\right\} \cdot \left[1 - \beta \cdot \frac{df_{\alpha'}}{d\varepsilon}\right] \quad (12.3)$$

Recently, the existing approaches have been extended by Wolf et al. [38, 41, 42] in order to be able to model the behavior of highly metastable CrMnNi steels with low SFE by incorporating their temperature and strain rate dependence. They used the flow stress data of 16-6-6 steel in the strain rate regime 10^{-3} to 10^{3} 1/s and included the effect of thermal softening as a function of strain and strain rate. Of particular note is that the flow behavior of the martensitic phase was characterized at different temperatures and strain rates (see Fig. 12.4). Due to the low carbon content of the 16-6-6 alloy, the martensite phase received excellent ductility under compression loading up to 10^{0} 1/s. This was most likely also promoted by a few volume percent of unavoidable residual austenite. With increasing strain rate the flow stress of the martensite increased, but the influence of thermal softening also increased in significance up to adiabatic shear banding at 10^{3} 1/s.

For the formulation of the model, it was first necessary to represent the strain rate dependence of yield strength and strain hardening of the two phases austenite and martensite. To describe the yield stress, the technical proof stress values at 0.2% compression strain were used whose strain rate dependence for both phases can be described by the following logarithmic relationships[4] [38]:

$$\sigma_{d0.2}(\gamma) = \sigma_{d0.2}(\dot{\varepsilon}_{\text{ref}}) + (0.954 \cdot \ln(\dot{\varepsilon}) + 10.564) \cdot \ln\left(\frac{\dot{\varepsilon}}{\dot{\varepsilon}_{\text{ref}}}\right) \quad (12.4)$$

$$\sigma_{d0.2}(\alpha') = 16.094 \cdot \ln(\dot{\varepsilon}) + 1796.8 \quad (12.5)$$

[4] $\sigma_{d0.2}$ = proof stress value at 0.2% compression strain
$\dot{\varepsilon}_{\text{ref}}$ = reference strain rate (0.0004 1/s).

The strain hardening of a stable austenite phase could be described by (12.4), while no strain hardening was assumed for the martensitic phase based on the quasi-static results. In agreement with Narutani [40], the amount of strain caused by the martensitic phase transformation was also considered by the following correlation $\varepsilon_T = \alpha \cdot f_{\alpha'}$ with $\alpha = 0.12$. The introduction of a correction term was of particular importance in order to account for the dynamic softening caused by adiabatic sample heating.

For this purpose, a term was inserted, which originates from the well-known model of Johnson and Cook [43] [(12.6)[5]]. The amount of temperature increase originates from [44] with the extension by Meyer et al. [45].

$$\sigma_{\text{Mod}} = \sigma_{\text{Cal}} \cdot \left[1 - \left(\frac{\Delta T}{T_S - T_{\text{ref}}}\right)^m\right] \tag{12.6}$$

All the above considerations are included in the constitutive flow curve model of Wolf et al. [38] which is presented in (12.7). An estimation of the transformed volume fraction of α'-martensite $f_{\alpha'}$ can be done by using experimental data from magnetic measurements or on the basis of the model by Olson and Cohen [6], which is given in (12.8).[6]

$$\sigma_{\text{Mod}} = \left[\sigma_{d0.2}(\gamma) \cdot (\varepsilon + \varepsilon_T) \cdot f_\gamma + \sigma_{d0.2}(\alpha') \cdot f_{\alpha'}\right] \cdot \left[1 - \left(\frac{\Delta T}{T_S - T_{\text{ref}}}\right)^m\right] \tag{12.7}$$

$$f_{\alpha'} = 1 - \exp\left\{-\beta \cdot \left[1 - \exp(-\alpha \cdot \varepsilon)\right]^n\right\} \tag{12.8}$$

Figure 12.5 shows the modeled flow curves of 16-6-6 steel for three different strain rates in comparison with experimental data points. The accordance is very good and especially the curve crossing phenomenon at higher strain rates due to thermal softening effect is reproduced in the model. Thus, the goal could be achieved, to include the essential physical mechanisms of deformation in high-alloy CrMnNi TRIP/TWIP steels into a constitutive flow curve model. The underlying microstructural deformation mechanisms during high-speed loading are also of great importance and will be discussed more in detail below.

[5] σ_{Mod} = predicted flow stress with temperature correction
σ_{Cal} = calculated flow stress without temperature correction
T_S = melting temperature
T_{ref} = reference temperature at which the material is tested.

[6] α = parameter which defines the shear band formation with strain
β = parameter which defines the intersection of shear bands with strain
n = fixed exponent, which is fitted to the experimental data.

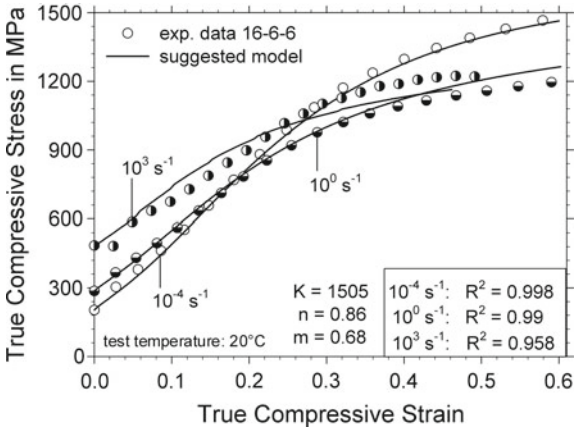

Fig. 12.5 Flow stress prediction of the developed constitutive model and experimentally determined flow stress data of 16-6-6 TRIP steel for three different strain rates [38]

12.2.3 Microstructural Deformation Mechanisms at High Strain Rates

As mentioned above, the primary deformation mechanism of TRIP/TWIP steels is the formation of planar defects such as separated Shockley partial dislocations, stacking faults or twins [8, 23, 24]. These mechanisms cause greater strength and strain hardening in comparison with wavy dislocation glide, which is active in common steel variants. The great particularity is the strong temperature dependence of these special deformation mechanisms, which means that the occurrence of glide planarity and martensite formation depends strongly on the respective environmental conditions during deformation. The investigations of Wolf et al. have shown that the same deformation mechanisms are active also in the high strain rate regime up to 10^3 1/s [25, 41, 42].

Figure 12.6 shows an example of the comparison of the microstructure of steel 16-6-6 after quasi-static compressive loading and dynamic compressive loading. In both cases, the microstructure of the deformed state up to 60% compression loading consisted of fine deformation bands and α'-martensite (cf. Fig. 12.6). Thin deformation bands evolved in the austenitic phase already at low strain values. With further straining, these deformation bands grew larger, crossed each other and α'-martensite nuclei were formed at their intersections. After quasi-static deformation the microstructure contained more and thicker bands, whereas after dynamic loading the bands appeared to be very thin and they were often oriented in one direction only. These findings were confirmed also by magnetic balance measurements, the results of which are already shown in Fig. 12.3b and indicated that an increasing strain rate caused a decreasing martensite formation due to adiabatic sample heating.

Generally, it is of great interest to use the additional deformation mechanisms, such as the TRIP- or the TWIP effect, since these lead to an increase in the energy

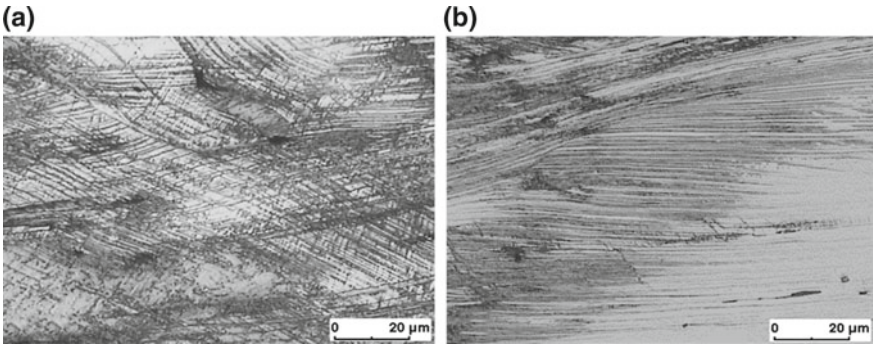

Fig. 12.6 Microstructure of steel 16-6-6 after deformation up to 60% compressive strain at strain rate of **a** 10^{-4} 1/s and **b** 10^{2} 1/s [25]

absorption capability of a material [25, 46] and thus, for example, to improved occupant protection in the event of impact in the automotive sector. Borisova et al. have shown that the high energy absorption results from interactions between individual microstructure defects with complex defect structures in which the formation of stacking faults can absorb approximately 1/30 of the whole deformation energy only [47]. Other essential absorption mechanisms include: (1) transition regions between ε-martensite and twinned austenite, (2) the formation of α'-martensite in deformation bands and (3) the formation of Lomer-Cottrell locks, stacking fault tetrahedra, and dislocation clusters. Nevertheless, the absorption of mechanical energy corresponds to the product of achievable strength level and the maximum ductility. Martin et al. showed that the strain hardening in TRIP/TWIP steels results from a continuous fragmentation of the dislocation mean free path due to deformation bands, stacking faults or the nucleation of α'-martensite [23]. A comparative consideration demonstrated that α'-martensite (G/25)[7] has a higher work hardening capacity than twins (G/50) in the austenite. However, the tensile elongation contribution is much more pronounced when twinning occurs. Huang et al. measured the greatest increase in ductility as soon as a high degree of glide planarity occurred, that means the occurrence of separated dislocations, stacking faults or austenite twins [48]. By contrast, the increase in tensile elongation due to α'-martensite formation was at best only 1/4 of that due to twinning.

As shown above, both the temperature dependence and the strain-rate dependence of the mechanical properties are important factors if the use of TRIP/TWIP steels for dynamically loaded components is considered. When the strain rate is further increased up to 10^{4} 1/s or above, the deformation and stresses are characterized by the propagation of elastic and plastic waves through the material. The deformation over the entire specimen cannot longer be considered as equilibrium, because stresses are transferred between several atomic layers, similar to a pulse with a length of only a few nanoseconds. Iron and steels have been subject to numerous shock wave studies

[7] G = shear modulus.

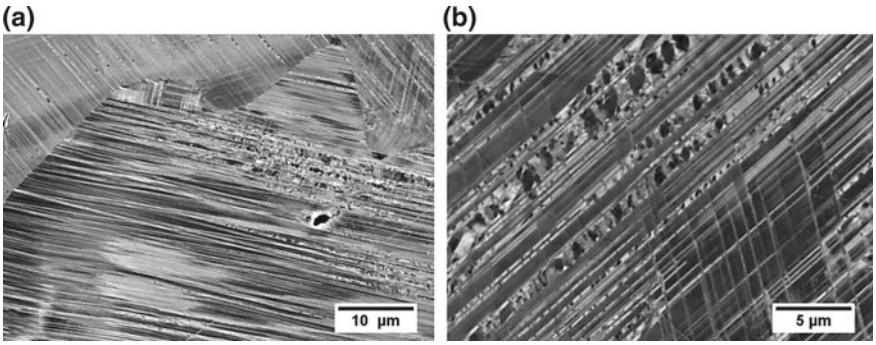

Fig. 12.7 SEM micrographs of the post-shock microstructure: **a** deformation band contrasts from backscattered electrons; **b** lenses within the bands indicate α'-martensite. The loading direction was vertical [20]

in the past. Especially the polymorphic phase transformation in iron from α-Fe to ε-Fe has been investigated extensively [49, 50]. However, in alloys with low stacking fault energy, e.g., in austenitic stainless steels, shock waves can cause additional martensitic transformations. Several studies have been carried out on steels corresponding to the composition of AISI 304 (~18% Cr, 8% Ni) under strain rates up to 10^5 1/s [51, 52]. On this occasion, the results confirmed the presence of the $\gamma \rightarrow \alpha'$ phase transformation up to such high loading rates. The microstructural changes comprised the formation of shear bands with a high concentration of deformation, whose intersections could act as nucleation sites for ε- and α'-martensite. Generally, shock prestraining led to increased microhardness and refined grains, due to high dislocation density and deformation twinning, which are both responsible for a strengthening effect [53].

Using the flyer-plate method, it was possible to identify the deformation mechanisms of CrMnNi TRIP/TWIP steels which are active under shock loading. Eckner et al. showed that an elastic-plastic shock wave produces a microstructure characterized by a high density of deformation bands, stacking faults and deformation-induced α'-martensite [20]. Figure 12.7 shows micrographs of this microstructural features, whereby the bands are clearly visible in BSE contrast. The grains had different deformation band densities and orientations, depending on the orientation to the load axis. Preferentially, their sites of origin were on active {111} slip planes of the face-centered cubic crystal lattice, due to the highest shear stresses under plastic deformation. Within the bands and at their intersections, α'-martensite was recognizable as small lenses. In accordance with results of quasi-static measurements, it could also be demonstrated that the driving force for the martensite formation increased at low temperature shock loading [20].

In order to demonstrate the deformation mechanisms, detailed TEM analyses were subsequently performed on the test samples [54]. It became clear that the austenite retained a high defect density through the plate impact and exhibited fine band structures. Intersection points of the deformation bands preferably showed

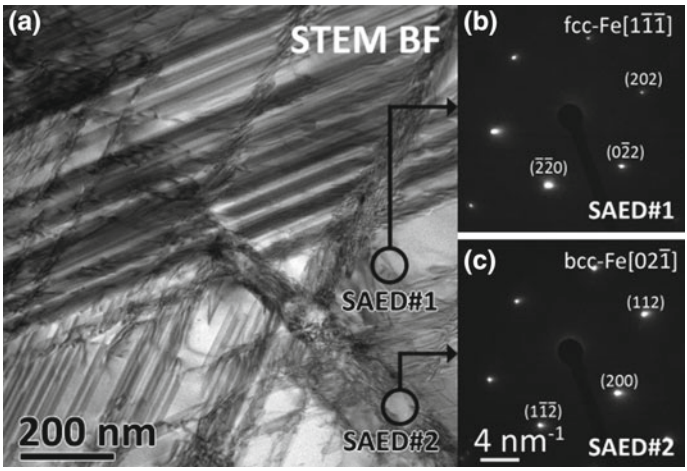

Fig. 12.8 Scanning TEM-micrograph of closely spaced deformation bands (**a**) in three different orientations (slip systems) within the γ-phase (**b**). The band intersections acted as nucleation sites for the formation of bcc α′-martensite (**c**) [54]

α′-martensite islands. At high magnification of the bands, their structure became clear as an arrangement of numerous parallel stacking faults or planar defects. In areas with high stacking fault density, it could be shown that α′-martensite was formed as assumed at the crossing points of the stacking fault bands. Figure 12.8 shows the STEM image of such a region. The enlargement of a nodal point of broader deformation bands shows that areas of the body-centered cubic phase have formed there. Using selected area electron diffraction (SAED), the lattice structure could be detected. In the area of the intersection point, the image contrasts indicated a very high defect density in the material. As reported by Martin et al. [23], the formation of α′-martensite nuclei led to the obstruction of the dislocation movement within the deformation bands and the accumulation of dislocations at the phase boundaries. In addition, the volume increase associated with the phase transformation caused a certain stress field around this area. However, the austenite outside of the bands was less deformed and parallel stacking faults could be detected here occasionally.

In the present case, the signal of the VISAR system was used to determine the characteristic strength values in the plate impact tests. A typical free surface velocity history, acquired during flyer-plate impact testing, is shown in Fig. 12.9a for the metastable austenitic CrMnNi16-6-6 cast steel. The wave form obtained was rather typical for elastic-plastic material behavior, and contained information about the yield point and the fracture strength. Initially, the elastic precursor arrived at the free end, which determined the Hugoniot elastic limit (HEL). Thereafter, the surface velocity increased again, which was associated with plastic deformation and ended in the steady Hugoniot state. The subsequent drop in surface velocity was due to the release wave or rarefaction, which reduced the pressure on the material and led to

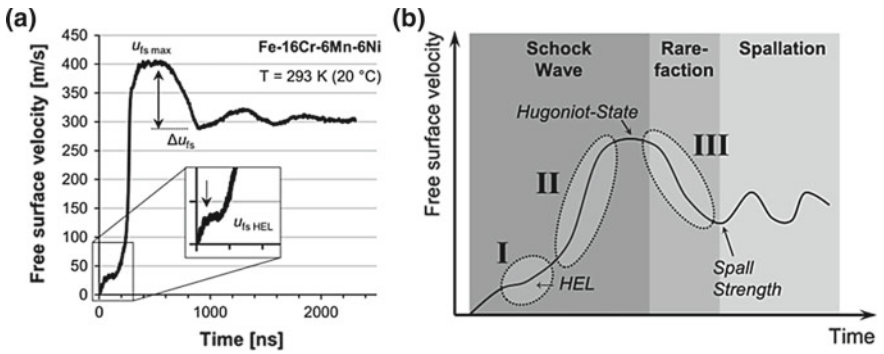

Fig. 12.9 **a** Free surface velocity profile of 16-6-6 cast steel impacted by an aluminum flyer plate at room temperature; **b** Schematic representation of the deformation mechanisms of metastable austenitic TRIP/TWIP steel during different loading states under flyer-plate impact [54]

spall fracture. The velocity pullback (Δu_{fs}) was used to determine the spall fracture strength.

Figure 12.9b presents a scheme of the deformation mechanisms of metastable austenitic TRIP/TWIP steel during shock wave loading, which was developed on the basis of the above shown experimental results of the microstructure analysis [54]. In stage I, at the very beginning of the shock deformation, elastic deformation and localized microplasticity occurred, based on the nucleation of stacking faults and thin deformation bands (planar dislocation glide). Slip occurred on several intersecting and closely-spaced planes, due to the very thin shock front and the uniaxial strain during the compression wave. In the following stage II, progressive strain hardening developed, due to a static and dynamic Hall-Petch effect caused by partial dislocation separation, slip band formation, increasing deformation band density and the formation of ε-martensite and α'-martensite nucleation sites. After the steady state (Hugoniot state), in stage III an expanding wave followed the shock wave, which reduced the materials density. The occurring tensile stresses promoted the $\gamma \rightarrow \varepsilon \rightarrow \alpha'$–transformation through an increase in formation and intersection probability of deformation bands with subsequent martensite nucleation and growth. Internal cavitation occurred, due to stresses generated by the interaction of stress waves which exceeded the local dynamic tensile strength of the steel. The coalescence of the cavities created a fragment (spall) which was finally separated from the free end of the plate.

Generally, this scheme of deformation mechanisms is also applicable to low or high temperature; however, there are various peculiarities that need to be considered here. Under shock conditions below room temperature, the thermodynamic driving force for the $\gamma \rightarrow \alpha'$–transformation increased strongly. This generally led to an increase in the strength characteristics of metastable austenitic steels, while at the same time the deformability was reduced. In addition, when the temperature fell below the M_S temperature (at about 1 °C for the CrMnNi 16-7-6 cast steel [14]), the α'-martensite also formed athermically, i.e. without the contribution of a mechanical

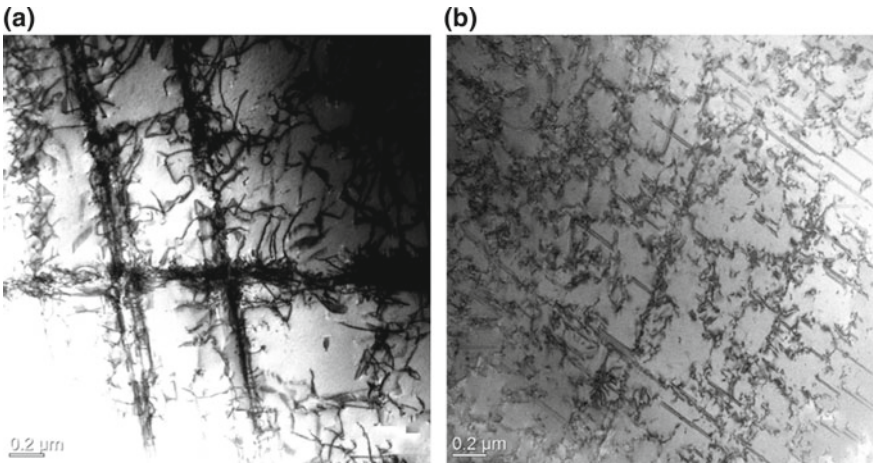

Fig. 12.10 Scanning TEM-micrographs of defect structures in CrMnNi16-6-6 steel after flyer-plate impact at **a** 100 °C and **b** 200 °C

deformation. Here, in addition to the deformation band structures already present at room temperature, coarse laths appeared within the microstructure, which also had a needle-like internal structuring. This was the cooling martensite or lath martensite, which is predominant in steels with <0.4% carbon. Similar martensite blocks can also be easily formed without further deformation in a simple cooling test. In general, the structure of the samples deformed at low temperatures was characterized by a very high density of deformation bands, which were evenly distributed over the entire inner sample area.

Furthermore, the more detailed analysis of samples tested at 100 °C and higher test temperatures showed partly fine deformation bands without significant α'-martensite nuclei at their intersection points. Also signs for wavy glide could be found, which is typical for face-centered cubic steels at high temperatures or materials with high stacking fault energies. Figure 12.10 shows exemplifying TEM images from the generated microstructures after plate impact at high temperatures. From previous investigations it is known that the deformation mechanisms change with increasing test temperature for the TRIP/TWIP steel investigated here [8]. Consequently, at 100 °C, the mechanical twinning or TWIP effect was a primary deformation mechanism also under shock loading. Moreover, there was a simultaneous occurrence of stacking fault bands (see Fig. 12.10a) and twins, which was not uncommon, since the movement of partial dislocations is a prerequisite for the occurrence of the TWIP effect [55]. Still, ε-martensite was identifiable at a low level after 100 °C shock loading, whereas nuclei of α'-martensite were only very rarely recognizable. The shock loading at 200 °C caused only a small degree of the occurrence of planar defects in the microstructure (see Fig. 12.10b). At such a high deformation temperature, it was to be expected that the deformation proceeds primarily due to dislocation glide. The

separation width of partial dislocations can only be small, due to the increased stacking fault energy. As a result, only isolated stacking fault contrasts could be found and twins were also extremely rare in this temperature range.

12.3 Honeycomb-Like Structures Made from TRIP-Steel and TRIP-Matrix-Composites

The introduction of novel cellular materials in crashworthiness-related fields of application requires a characterization of structure response and microstructure evolution in the cell wall material as a function of different parameters. In the following sections, the influence of the loading direction and the cell wall composition on the strength, deformation and damage behavior of honeycomb-like structures will be discussed in detail. Closer information about the effects of an altered test temperature and strain rate can be found in [12, 56–58].

12.3.1 Deformation Behavior of Honeycomb-Like Structures

The periodic 2D arrangement of unit cells in the investigated honeycomb-like structures results in an anisotropic material behavior which makes a distinction into two load modes necessary. The Out-Of-Plane (OOP) mode indicates the application of load parallel to the channel axis, defined as the $X3$-direction in Fig. 12.11, whereas in In-Plane (IP) mode the load is applied parallel to the $X1$–$X2$ plane.

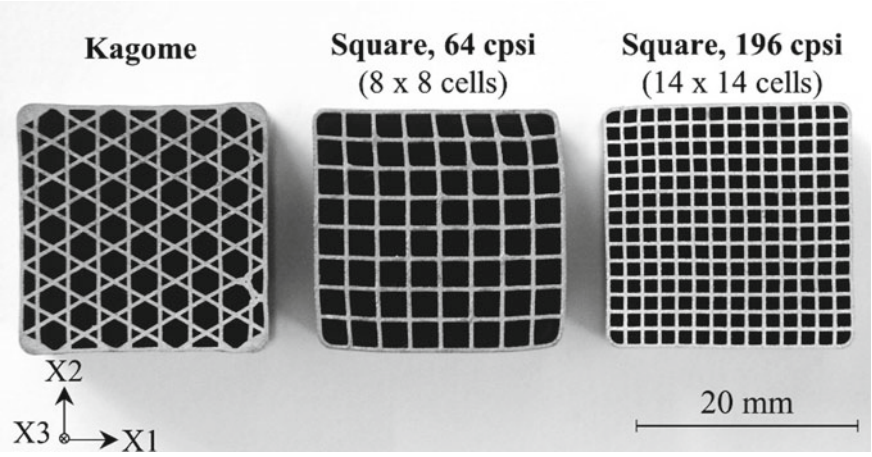

Fig. 12.11 Cross-section of investigated honeycomb-like structures in sintered state

In order to investigate the differences of OOP and IP deformation behavior, compression tests on samples with an approximate aspect ratio of 1:1 were conducted. Mechanical machining on the front sides ($X1$–$X2$ plane) ensured the desired sample dimensions and the orthogonal alignment of the cell walls, especially in OOP mode. The use of servohydraulic universal testing machines with load cells of 250 and 500 kN served for testing at quasi-static strain rates. Subsequent microstructural investigations on the deformed samples, using light optical microscopy and scanning electron microscopy in connection with EDX- and EBSD-measurements, supported the identification of the effective deformation mechanisms in the TRIP-steel matrix and the Mg-PSZ particles. The quantification of ferromagnetic α'-martensite evolution was realized by magnetic balance measurements at the beginning of the project and later continued with a MSAT magnetic saturation device.

Table 12.2 gives an overview on the TRIP-steel batches which were used for comparing the OOP and IP deformation characteristics and analyzing the effect of an altered cell wall composition. In addition, the table contains the calculated chromium and nickel equivalents, the stacking fault energies according to [59] and the additional constituents of the MgO partially stabilized zirconia.

12.3.1.1 Out-of-Plane Direction

The compressive deformation in OOP direction causes a stretch-dominated deformation mechanism in the honeycomb-like structures. Initially, the cell walls are elastically compressed until the yield strength is exceeded. With increasing compression a distinct strain hardening takes place characterized by a continuous rise in stress. In agreement with the observations of Côté et al. [60], the flow curve incline of a cell wall of the honeycomb-like structures and the respective bulk material are similar up to certain strains in this deformation stage called pre-buckling region. However, the offset in the absolute stress value derives from the varying microporosity amounting up to 15% in the struts of the cellular materials [57]. A higher microporosity results in reduced strength and deformation values, as discussed by Bocchini et al. [61].

The point of deviation in flow curve incline of cellular material from bulk material identifies the onset of structure bifurcation and hence the transition from stable to instable plastic deformation. With the onset of this post-buckling stage, progressive damage processes in the cell walls lead to a reduced strain-hardening potential. As a result, a stress maximum is formed. Within the ensuing deformation range, the buckled and fractured cell walls are compressed by an almost constant force until contacts between neighboring cell walls are formed. The densification of the entire structure involves a steep stress increase. Principally, all the investigated honeycomb-like structures display these characteristic deformation stages. However, the relative density $\bar{\rho}$ of the structures has a great influence on the achievable strength level and the strains at which a transition in deformation behavior occurs [12, 62].

Table 12.2 Overview of steel alloying elements and additional constituents of MgO partially stabilized zirconia in wt%

Batch	Abbr.	Cr	Mn	Ni	C	N	Si	Mo	Cr_{eq} [13]	Ni_{eq} [13]	γSFE[a]
X1CrNi 18-9	18-1-9	18.4	1.1	9.3	0.009	0.127	0.67	0.028	19.4	12.4	23
X3CrMnNi 17-8-10	17-8-10	16.6	7.7	10.1	0.025	0.065	1.17	0.002	18.4	15.9	19
X3CrMnNi 16-7-7	16-7-7	16.3	7.2	6.6	0.030	0.088	1.00	0.007	17.8	12.7	14
X3CrMnNi 17-7-6	17-7-6	17.0	6.5	6.1	0.030	0.082	0.30	<0.01	17.5	11.7	16
X5CrMnNi 17-7-3	17-7-3	16.7	7.1	3.4	0.050	0.097	0.91	0.024	18.1	10.2	9

[a] according to Dai et al. [59] $\gamma = 39 + 1.59\%Ni - 1.34\%Mn + 0.06\%Mn^2 - 1.75\%Cr + 0.01\%Cr^2 + 15.21\%Mo - 5.59\%Si + 26.27(\%C + 1.2\%N)(\%Cr + \%Mn + \%Mo)^{0.5} + 0.61(\%Ni(\%Cr + \%Mn))^{0.5} - 60.69(\%C + 1.2\%N)^{0.5}$

	MgO	SiO_2	HfO_2	Al_2O_3	CaO	TiO_2	ZrO_2
Mg-PSZ	3.4	2.4	1.7	0.6	0.2	0.1	Bal.

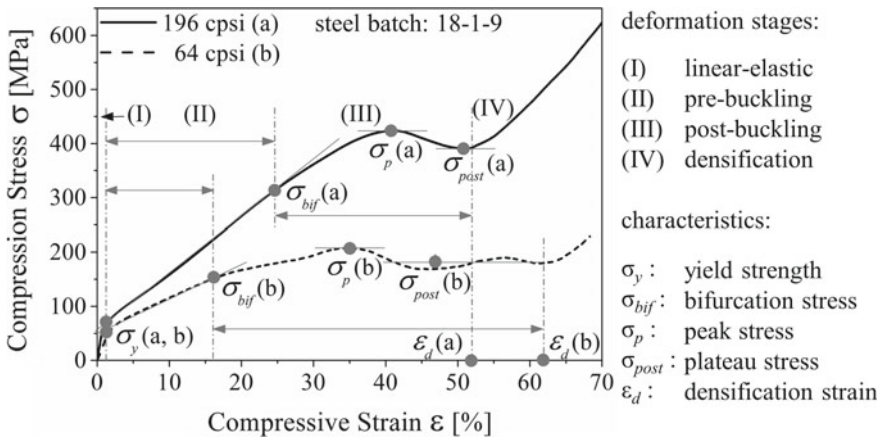

Fig. 12.12 Stress-strain curves of square-celled structures with 64 cpsi and 196 cpsi made from steel batch 18-1-9, compressed at quasi-static strain rates and room temperature [62]

An estimation of $\bar{\rho}$ for the square-celled structures can be made according to (12.9).[8] In addition, the ratio of global structure density ρ^* and density of the cell wall material ρ_s is also suitable to calculate this structure parameter [62, 63].

$$\bar{\rho} = \frac{\rho^*}{\rho_s} \cong (1 - p_m)\left[2\left(\frac{t}{l}\right) - \left(\frac{t}{l}\right)^2\right] \approx 2(1 - p_m)\frac{t}{l} \tag{12.9}$$

Both investigated square-celled structures have a comparable average cell wall thickness of approx. 300 µm (64 cpsi) and 320 µm (196 cpsi) and a residual amount of porosity in the cell walls due to the manufacturing process. However, the cell edge length differs considerably from approx. 2400–1500 µm resulting in relative densities of 0.24 and 0.36 [57]. Differences of these parameters in varying batches of honeycomb-like structures can be traced to an altered amount of microporosity and shrinkage. Figure 12.12 visualizes that minor strength is provided by the low-density structure over the whole deformation range. Besides, structural damages and the ultimate collapse identified by the peak stress are initiated at lower strains. In comparison to the 196 cpsi structure, a distinct stress plateau is developed in the cellular material with 64 cpsi prior to densification which takes place at higher strains. These tendencies conform with findings of other research groups [60, 63] reporting an increase of peak stress and a reduced densification strain with increasing

8 $\bar{\rho}$ = relative density
ρ^* = global structure density
ρ_s = density of the cell wall material
t = cell wall thickness
l = cell edge length
p_m = cell wall microporosity.

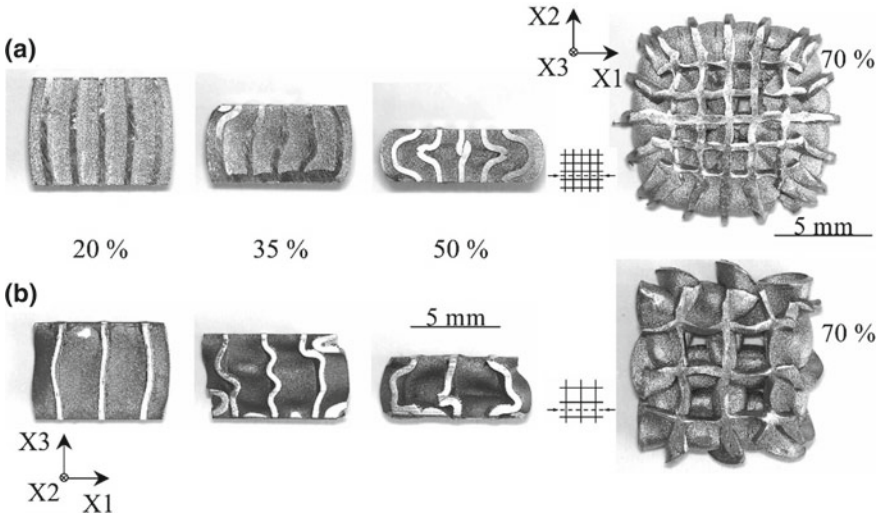

Fig. 12.13 Side view of buckling and failure patterns within the core of down-scaled samples made from steel batch 18-1-9 at different deformation stages and top view of 70% strained state: **a** 196 cpsi and **b** 64 cpsi structure [57]

relative density. However, the formation of a pre-buckling stage seems to be more common for steel matrix structures than for structures composed of aluminum [64]. Object of investigation is further the number of cells required to describe the stress-strain behavior properly. In order to assess this aspect, segments with 4 × 4 and 2 × 2 cells and an equal aspect ratio are cut out of the 196 cpsi and 64 cpsi structure, respectively. Quasi-static compression tests on the down-scaled samples demonstrate that no significant difference is recorded in the linear-elastic and pre-buckling stage. The absence of the stiffened outer skin causes only a slight shift of peak stress to lower strains, cf. [12, 57].

Interrupted compression tests serve to record the different macroscopic deformation mechanisms of the two structures. In the 196 cpsi sample, stable plastic deformation is accompanied by axial crushing and global buckling of cell walls within the $X1$–$X3$ and $X2$–$X3$ plane (cf. Fig. 12.13a). The radius of curvature increases with increasing compressive strain, until plastic kinks are built involving the onset of instable deformation. However, centered cell walls are restricted to deform freely due to the constraining effect of the outer elements. Hence, shear failure and fracture is promoted. In contrast to this global plastic "Euler-type" buckling, the low-density structures deform by local and torsional buckling which leads to folding collapse (cf. Fig. 12.13b) [57].

Sometimes the structures exhibit manufacturing related defects like cracks and inhomogeneities in the undeformed state which can be visualized by computer-tomographic investigations [65]. In order to generate a better comparability of batches

with a varying amount of imperfections the recorded stress is normalized to the relative density of the particular structure in the following sections.

12.3.1.2 In-Plane Direction

At the beginning of deformation, the stress-strain behavior in IP direction is determined by the elastic compression of cell walls similar to OOP mode. However, in case of the square-celled structures, the passing of compressive yield strength is closely linked to the compressive peak strength indicating that no stable plastic deformation within a pre-buckling stage takes place (Fig. 12.14). The subsequent steep stress decrease initiates the plateau stage which is characterized by an almost constant stress signal with only small oscillations and limited by structure densification [62]. By comparing the stress-strain response with the one in OOP mode, it is obvious that less mechanical work is required for IP deformation. An explanation is given by the macroscopic failure mechanism.

Ideally, the sintered honeycomb-like structures with square cells possess exactly aligned cell walls as predetermined by the employed die of the extrusion process. Therefore, the struts oriented parallel to the applied force, will be loaded with primarily axial stresses. As a result of the sintering process, cavities in the green bodies are more and more eliminated leading to a shrinkage of 10–15% [67]. Despite the occurrence of an almost homogenous shrinkage, small deflections of the cell walls cannot be excluded. These structural imperfections in addition to residual pores and cracks have a wider impact on IP deformation, because they are initiation points of instable plastic deformation. The onset is concentrated in the cell row with the highest deviation of structural integrity. Therefore, bending moments are initiated leading to cell wall rotation processes around adjacent cell nodes. In addition, the lattice design of the square-celled structure provides no sufficient transverse rigidity so that asymmetric shearing takes place with increasing strain, cf. Fig. 12.15. In contrast to

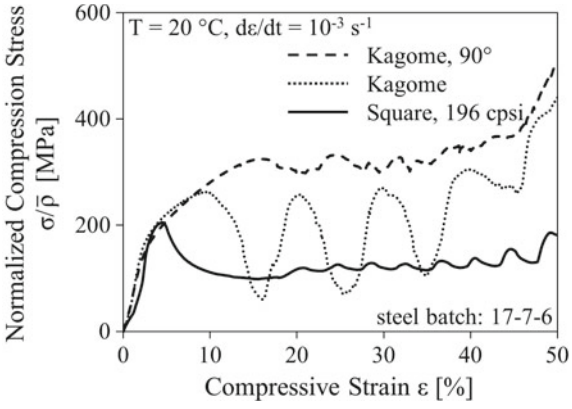

Fig. 12.14 Quasi-static stress-strain curves of Kagome (deformation in $X1$-direction), Kagome 90° (deformation in $X2$-direction) and square-celled structures recorded in IP mode according to [66]

Fig. 12.15 Deformation patterns of Kagome (deformation in $X1$-direction), Kagome 90° (deformation in $X2$-direction) and square-celled structures at engineering strains of 25% for IP mode and quasi-static strain rates according to [66]

OOP mode, where all three spatial directions are affected, IP plastic deformation is limited in the $X1$–$X2$ plane due to the 2D assembling of cells [62, 66].

In order to improve the IP properties of the honeycomb-like structures, altered cell designs are investigated by simulation on the basis of Finite Element Method (FEM) analysis [68]. Computation is conducted by the use of an isotropic, strain rate dependent and isothermal material model, based on true stress-strain curves of steel 18-1-9 and an explicit solver in ABAQUS. Nine main profiles serve as input files. For five of these profiles, a 90°-rotation is necessary to describe the whole mechanical behavior in IP mode due to the axial anisotropy of the lattice. The mass-specific (m) energy absorption capability as a characteristic value and integral information of the force (F)-displacement (s) curve is chosen to compare the performance of the investigated structures. It can be calculated as follows:

$$\mathrm{SEA}_m = \frac{\int_0^{s_i} F(s)\mathrm{d}s}{m} \tag{12.10}$$

As a result of the FEM analysis, the Kagome lattice, which consists of an ordered sequence of hexagons and triangles, provides superior properties compared to the square-celled structure. In OOP direction the relative increase of specific energy absorption capability is moderate whereas in IP mode the increment for both Kagome orientations is immense. The comparative experimental investigations of the Kagome and the square-celled lattice, both manufactured out of steel batch 17-7-6, serve to verify the results of the FEM analysis [66, 68]. In OOP mode the increase of static energy absorption capability of the Kagome configuration is no more than 2 kJ/kg at 40% engineering strain and hence less than 5% of the absolute value. However, in IP direction the static absorption capability of the Kagome structure loaded in $X2$-direction (denoted as Kagome 90°) is more than twice as much as that of the square-celled structure and in $X1$-loading (denoted as Kagome) a raise of approx. 70% is measureable. By considering the progression of the stress-strain curve in Fig. 12.14, a continuous raise of stress takes place after passing the transition point from elastic to plastic deformation for both Kagome alignments in contrast to the square-celled structure. Furthermore, the average stress level in the plateau stage is

higher than compared to the square-celled structure. Fundamental reason for the IP improvement is the change of deformation mechanism. As discussed in literature [69, 70], stretching-dominated cellular materials provide a higher stiffness and a greater strength as compared to bending-dominated structures. The latter mechanism is predominant in the square-celled structure due to the mentioned manufacturing-caused imperfections.

The deformation patterns are also in good agreement with the simulation. For both Kagome orientations, plastic deformation is symmetric with respect to the direction of loading, cf. Fig. 12.15. For $X1$–loading, the deformation pattern is characterized by buckling of angled lattice struts and cell wall rotation processes around adjacent cell nodes with increasing strain. A mainly triangle-shaped deformation pattern, which is formed by buckling of the vertical cell walls, defines the deformation in $X2$-orientation. At high strain levels a combination with upper deformation bands takes place.

12.3.2 Selection of Cell Wall Materials

Apart from the loading direction and the lattice design, the mechanical properties of honeycomb-like structures are significantly influenced by the characteristics of the cell wall material. In the following, the effect of nickel content in the steel matrix and the volume fraction of Mg-PSZ particles have been analyzed to demonstrate how the OOP deformation behavior of the 196 cpsi honeycomb-like structure can change.

12.3.2.1 Influence of Nickel Content

Metastable austenitic steels can respond to plastic deformation with different deformation mechanisms. The transformation from γ austenite into ε- or α'-martensite, called TRIP-effect, represents one possibility in addition to dislocation glide. Another alternative is the occurrence of mechanical twinning, called TWIP-effect. Decisive for the occurring mechanism are several parameters like chemical composition, stacking fault energy (SFE), temperature, stress state and strain rate, which can interact with each other [8, 25, 71–74].

Principally, a spontaneous transformation of austenite into martensite is possible if the difference in Gibbs free energy of both phases exceeds a certain threshold value below the martensite start temperature M_s. However, in plastically deformed TRIP-steels an amount of mechanical work can be added to the chemical driving force causing the start of martensite nucleation to shift to temperatures above M_s. The upper limit for deformation induced martensite formation is determined by the M_d temperature. At this temperature, the applied load is still sufficient to generate the critical shear stress in order to form 1 vol% of α'-martensite [7, 75].

Whether the selected steel is able to show the TRIP-effect and how great the extent will be, strongly depends on the austenite stability which is affected by the

chemical composition. Alloying elements like carbon, nitrogen, nickel and manganese promote the stability. The weighting of their influence is contained in the equation of the nickel-equivalent, cf. (12.11) in wt% [13]. In connection with the chromium equivalent, a classification within the Schaeffler-diagram is possible and hence the estimation of microstructure constitution for a given chemical composition at room temperature in the undeformed state. The closer the alloys are situated at the separation line of the single phase austenite and the two-phase austenite/martensite region in this diagram, the greater the tendency for a deformation induced phase transformation. The nickel-equivalent can also be employed for the estimation of M_s as Jahn et al. [76] demonstrated on the basis of dilatometer measurements on CrMnNi steels with varying chemical composition. According to this, M_s shows a parabolic increase with decreasing Ni_{eq}, which is closely associated with a reduction of austenite stability.

$$Ni_{eq} = \%\ Ni + 30\%\ C + 18\%\ N + 0.5\%\ Mn + 0.3\%\ Co + 0.2\%\ Cu\ - 0.2\%\ Al \quad (12.11)$$

Another parameter with great impact on the occurring deformation mechanism is the SFE which is a function of chemical composition and temperature [8, 59]. Austenitic steels with a low SFE possess Shockley partial dislocations with a great split-up implying that recombination of partial dislocations is not favored. For this reason, plastic deformation is dominated by planar glide and localized in deformation bands. With increasing strain, the amount of stacking faults on every second {111} plane increases and hcp ε-martensite therefore can be measured [77]. Furthermore, more and more nucleation sites for the α'-martensite transformation are built by the intersection of these deformation bands in addition to an increasing stress level which finally exceeds the triggering stress [75]. Austenitic steels with high SFE require a high stress to separate partial dislocations and form large stacking faults. Besides, the energy barrier for the ε-martensite formation increases and thus the formation of an hcp structure becomes unfavorable from the thermodynamic point of view [78]. As a consequence, stacking faults are generated on every successive {111} plane leading to the formation of mechanical twins (TWIP-effect) [79]. Regarding the nature of glide in steels with high SFE, lower stresses have to be applied to cause a recombination of partial dislocations. Therefore, cross-slip is possible resulting in a lower strain hardening potential. At a certain amount of SFE, plastic deformation proceeds by pure dislocation glide since the stress level required for the separation of partial dislocation exceeds the fracture strength of the steel.

Martin et al. [8, 73] conducted microstructural investigations on CrMnNi samples deformed at different temperatures. Since the variation in temperature is accompanied with a change in SFE energy, they extrapolated the SFE under the assumption that the SFE increases by 0.075 $mJK^{-1}\ m^{-2}$. Therefore, SFE ranges with characteristic deformation mechanisms could be proposed. Above 40 $mJ\ m^{-2}$ pure dislocation glide is prevalent whereas between 20 and 40 $mJ\ m^{-2}$ pronounced deformation twinning occurs. For energies below 20 $mJ\ m^{-2}$, a continuous transition to ε- and α'-martensite formation takes place which is always supported by dislocation glide.

In Fig. 12.16 the effect of varying deformation mechanisms within the steel matrix is displayed for the square-celled 196 cpsi honeycomb-like structures. Mayor difference of the investigated samples is the nickel content which influences the nickel equivalent and the stacking fault energy, as Table 12.2 reveals.

The graph shows that the compressive yield strength increases by decreasing the nickel content. Furthermore, plastic deformation in the pre-buckling stage generates the highest flow stress and the greatest strain-hardening in the honeycomb-like structure containing 3 wt% nickel, followed by the 7 wt% nickel sample. However, considering the onset of structure bifurcation and the start of softening due to immense structural damages at the peak stress, a decreasing triggering strain with decreasing nickel content becomes obvious. Nevertheless, the stress level of 3 and 7 wt% nickel containing samples is still higher in comparison to the sample with 10 wt% nickel. Consequently, the area enclosed by the stress-strain curve, which correlates with the energy absorption potential of the structures, decreases with increasing nickel content. Interrupted compression tests in combination with MSAT-measurements served to monitor the evolution of α'-martensite in

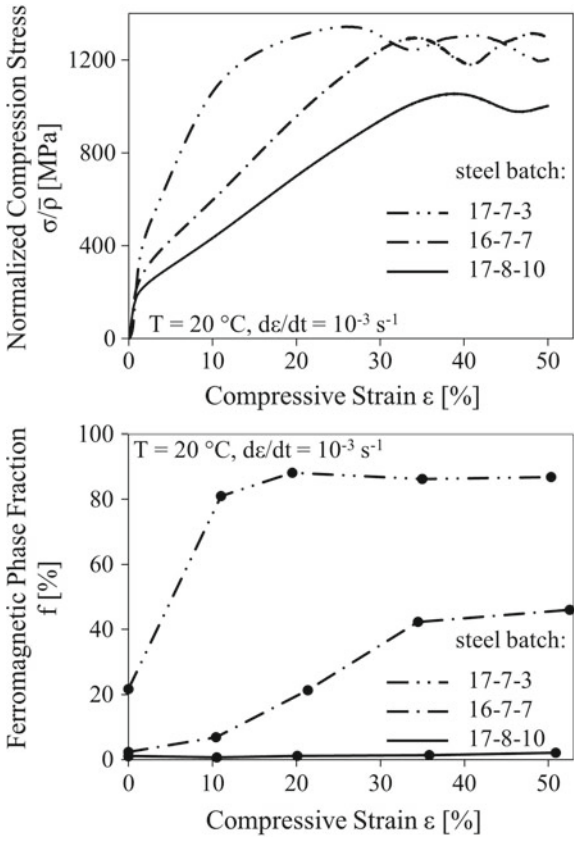

Fig. 12.16 Stress-strain behavior and α'-martensite evolution of CrMnNi square-celled honeycomb-like structures with varying nickel contents deformed in OOP mode, data used from [46]

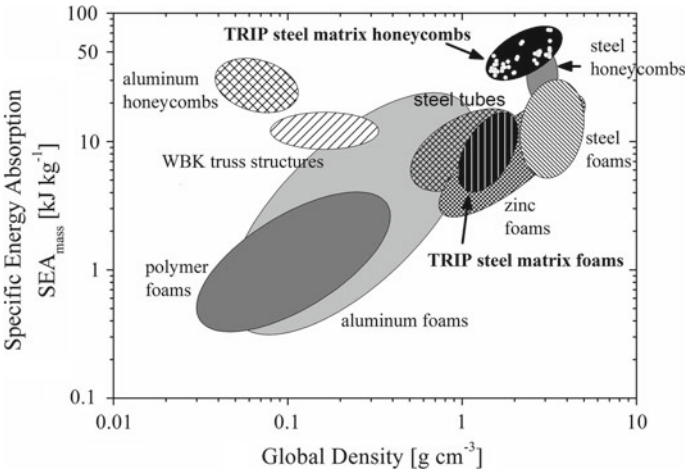

Fig. 12.17 Comparative overview of mass specific energy absorption of TRIP-steel matrix honeycombs and other structures according to [12], additional results of samples made from 17-7-3, 16-7-7 and 17-8-10 steel batches have been added (each single white dot refers to one single measurement result)

the structures, cf. Fig. 12.16. As expected, the highest amount of deformation induced α'-martensite is found in the 3 wt% nickel sample possessing the lowest Ni_{eq} and the lowest SFE. At 20% engineering strain the saturation content of α'-martensite is already reached. Due to the small amount of interstitial alloying elements, the lattice distortion and hence the strength of the α'-martensite islands is comparatively low. Nevertheless, α'-martensite is an effective obstacle regarding dislocation movement which contributes to a distinct strengthening effect [24]. The high driving force for the TRIP-effect in the 3 wt% nickel structure results, however, in the restriction of deformation capacity. Similar observations are made in the related bulk material, cf. uniform/fracture elongation [72].

In the 7 wt% nickel containing sample, the TRIP-effect is less dominant as indicated by the lower absolute ferromagnetic phase fraction. Besides, it becomes obvious that a higher amount of plastic strain is necessary to achieve the saturation content of α'-martensite in these samples. Microstructural investigations visualize that α'-martensite has an oval lense-shaped appearance and forms within deformation bands. Increasing the nickel content up to 10 wt% shifts the deformation mechanism to ε-martensite formation and mechanical twinning (TWIP-effect). Therefore, no significant ferromagnetic content is measureable even at 50% engineering strain. The microstructure images prove that an increased amount of stacking fault arrangements is contained in the samples but no α'-martensite is recognizable [46].

In order to classify the obtained results, the energy absorption performance of the honeycomb-like samples (196/64 cpsi) at 50% engineering strain is compared to several other structures, cf. Figure 12.17. All considered data refer to quasi-static compressive loading and to OOP mode in case of honeycomb(-like) structures and

tubes. The TRIP-steel matrix honeycombs belong to the cellular materials with high global density, but they still provide a great mass specific energy absorption capability. The TRIP-steel matrix honeycombs based on the initial 18-1-9 steel batch already exhibit a maximum absorption capability of 54 kJ/kg, as presented in [12]. With introduction of the 16-7-7 and 17-7-3 steel generation, the energy consumption can be further increased up to 74 kJ/kg, due to the higher driving force for the deformation induced martensitic phase transformation leading to an enhanced strength level. However, the honeycombs made from steels with a lower austenite stability are more prone to structural softening as a result of quasi-adiabatic sample heating even at strain rates of 10^2 1/s. Curve crossing phenomena of statically and dynamically deformed samples are shifted to lower strains which is also valid for the bulk material [33, 46]. Therefore, it has to be considered that the dynamic energy absorption capability can adapt or can fall even below the quasi-static one at elevated strains [25].

12.3.2.2 Effect of Particle Reinforcement

The addition of MgO partially stabilized zirconia particles in the TRIP-/TWIP-steels is intended to increase the strength of the composite which bases on several mechanisms. On the one hand, external applied loads are supposed to be transmitted from the matrix through the interface to the stronger ceramic. Additionally, the different ductility of the components and the misfit due to the varying crystal structures contribute to an increase in strength. On the other hand, an indirect strengthening mechanism results from the different coefficients of thermal expansion. During cooling from processing temperature, the steel contracts stronger in comparison to the ceramic so that dislocations are generated at the interfaces and the material is subjected to strain hardening. In principle, the effectiveness of the mechanisms depends on the volume content, the shape and the orientation with respect to the load direction of the reinforcing phase [80].

Apart from the described mechanisms, which are the basis for all metal matrix composites (MMC) with superior strength properties, the Mg-PSZ particles are supposed to contribute to further strengthening by a martensitic phase transformation. At initial state the particles exhibit a cubic/tetragonal microstructure which transforms into monoclinic state by mechanical loading in connection with exceedance of the triggering stress. The transformation is accompanied by a volume expansion generating an additional amount of compressive strain in the surrounding matrix. Hence, more mechanical work is available for the TRIP-effect in grains with a favorable orientation. Martin et al. [81] proved the occurrence of this interaction and its positive effect on the mechanical properties by comparing MMCs reinforced with 5 vol% Al_2O_3 and Mg-PSZ, respectively. The greatest flow stress in the whole deformation range was provided by the Mg-PSZ sample although the content of α'-martensite was lower as compared to the non-reinforced sample. This fact was explained by the limited deformability in the ceramic which restricts plastic flow in the TRIP-matrix. However, an increase in monoclinic phase fraction with increasing strain

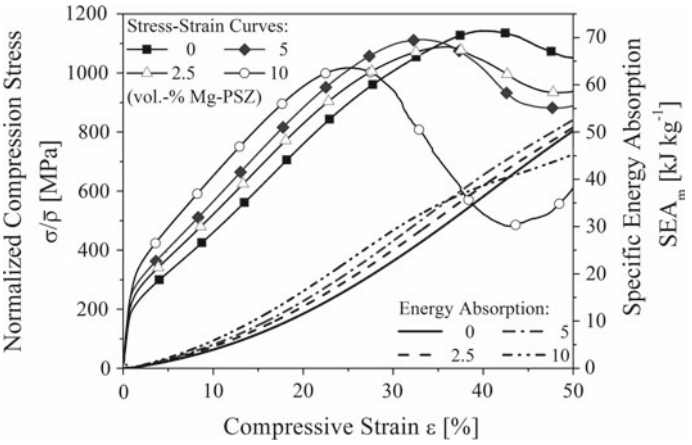

Fig. 12.18 Quasi-static stress-strain response of 196 cpsi honeycomb-like structures composed of 18-1-9 steel batch with 0 to 10 vol% Mg-PSZ particles, data used from [67]

was detected and more α'-martensite was measured in the Mg-PSZ sample than in the one containing Al_2O_3.

In order to exploit the whole potential of these mechanisms, the amount of monoclinic phase has to be reduced at initial state. For bulk material, synthesized by Spark Plasma Sintering, this precondition can be ensured as the results of Krüger et al. [10] demonstrated. However, the honeycomb-like structures are manufactured by conventional sintering which requires high temperatures and long dwell times to receive dense products. The manufacturing parameters permit diffusion processes both in direction of the steel and the other way around, as Berek et al. [82] reported. As a consequence, magnesium reacts to silicates and spinels with alloying elements of the steel and is no longer stabilizing the ceramic in the cubic/tetragonal phase. However, Weigelt et al. [83] observed that exposing pure Mg-PSZ to temperatures of 1300 °C, which is close to the tetragonal → monoclinic phase transformation temperature, resulted also in a significant decrease of stabilized cubic/tetragonal phase even without a steel interaction. At initial state 90% of the Mg-PSZ microstructure was of cubic/tetragonal phase whereas only 30% remained after firing at 1300 °C for 3 h. Elevating the sintering temperatures to 1400 °C was favorable for a greater cubic/tetragonal phase content, but is close to the melting temperature of the steel. Consequently, the strengthening effect of the martensitic phase transformation within the Mg-PSZ is comparatively low in conventionally sintered honeycomb-like structures [84].

The effect of different Mg-PSZ volume contents, varying between 2.5 and 10 vol%, on the OOP deformation behavior of square-celled 196 cpsi honeycomb-like structures is depicted in Fig. 12.18. In accordance with the mechanical response of the related bulk material, the compressive yield strength of the honeycomb-like structures increases with increasing amounts of Mg-PSZ [57]. The enhancement of

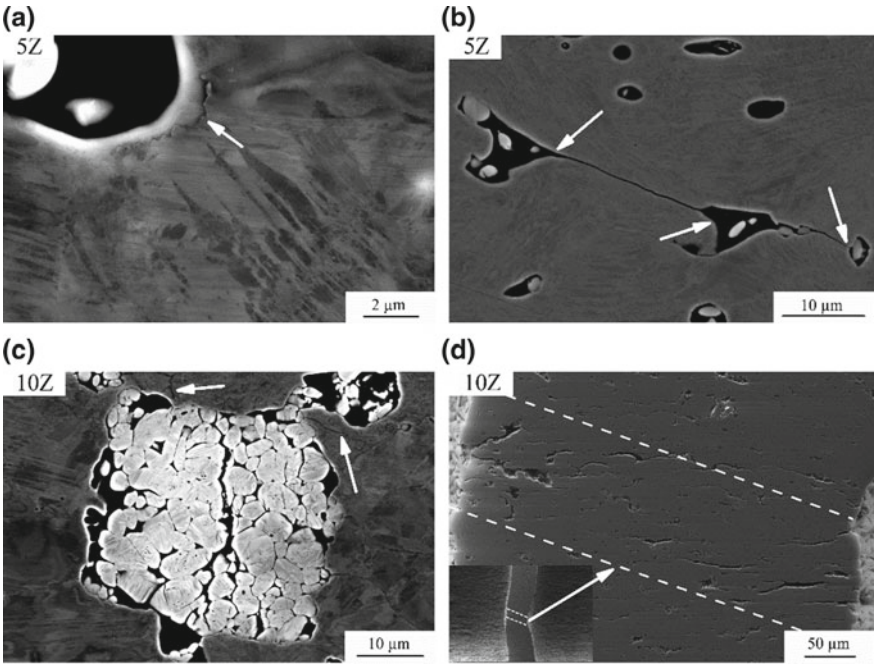

Fig. 12.19 Damage processes of TRIP-Matrix-Composites according to [62] at $\varepsilon = 20\%$ **a** interface debonding, **b** crack bifurcation at particles and pores, **c** failure of Mg-PSZ agglomerate as well as matrix cracks and **d** weakened cell wall cross-section at $\varepsilon = 35\%$; Z denotes vol% Mg-PSZ

plastic compression stress and work hardening rate continue up to certain deformation stages in the pre-buckling stage due to a constrained plastic flow in the matrix arising by the presence of the rigid ceramic particles. In addition, the polygonal shape of the Mg-PSZ leads to stress concentrations at the interfaces between matrix and particle, possessing a perpendicular orientation to the loading direction. Depending on the crystal orientation of the surrounding austenitic grains, more dislocations can form, further glide systems can be activated and an increased ε- and α'-martensite formation is possible [81]. It is obvious that the more particles are contained the greater the impact of these mechanisms on the resulting strength.

However, the increasing inhomogeneous stress distributions can finally exceed the steel/ceramic interfacial strength and the fracture strength of the steel matrix, respectively. Debonding processes and crack initiation are the result, visualized by Fig. 12.19a. Additionally, the fracture of brittle ceramic particles, cracking of Mg-PSZ agglomerates and crack bifurcation contribute to material softening processes, cf. Figure 12.19b, c. Hence, with increasing Mg-PSZ content a lower crush resistance (maximum strength) is provided and failure shifts to lower strains, cf. Figure 12.18. The steeper stress decrease of the composite structures within the post-buckling stage arises by the formation of micro crack networks which can combine to macro cracks. Especially areas with high particle density and great strain localizations are prone to

cracking which is accompanied with particle rearrangement processes. As a result, Mg-PSZ particles are lined up in unattached cluster chains leading to a weakening of the cell wall cross section, cf. Figure 12.19d.

The sum of damage processes is adverse for the α'-martensite evolution as the measurements of ferromagnetic phase content reveal. At low engineering strains (up to approx. 10%), partially higher α'-martensite contents can be identified in the central deformation areas of the composite honeycomb-like structures whereas at 50% engineering strain the highest α'-martensite content within the same area is found in the non-reinforced sample [62, 67]. Nevertheless, the reinforcement of TRIP-steel with Mg-PSZ particles can contribute to an increased energy absorption capability up to 50% engineering strain as the comparison of the non-reinforced and the 5 vol% Mg-PSZ containing sample in Fig. 12.18 shows.

Thus, the main finding—likewise on basis of other employed steel batches—is the increase of energy absorption capability by reinforcing the steel with Mg-PSZ particles being most effective for low strains where material damages are not pronounced [46].

12.4 Conclusions

The material behavior of metastable TRIP-steels was investigated in the form of bulk material and honeycomb-like structures. Strain-rate and temperature dependent compression tests with subsequent microstructural investigations on the bulk samples led to the following findings:

- In dependence of the deformation temperature different deformation mechanisms are dominating: below 100 °C the deformation-induced formation of ε- and α'-martensite, between 100 and 250 °C mechanical twinning and above 250 °C dislocation glide.
- An own model was presented to describe the material behavior under consideration of the strain rate sensitivity of austenite and martensite, adiabatic heating and strain hardening of the austenite. The model, which is based in a modified rule of mixture, provides excellent results.
- The dominant deformation mechanisms of the 16-6-6 CrMnNi steel in the strain rate range of 10^{-3} up to ~5×10^4 1/s were the accumulation of stacking faults in lamellar deformation bands and the strain-induced formation of ε- and α'-martensite. Low temperatures raised the driving force for α'-martensite formation also in shock loading. The particularly high strain rates during flyer-plate impact induced α'-martensite formation even at very low strains. However, the $\gamma \rightarrow \varepsilon$ transformation still occurred as an intermediate step.

Compression tests on honeycomb-like structures in dependence of loading direction, nickel content in the steel and volume content of Mg-PSZ can be summarized as follows:

- In OOP mode the cell walls were exposed to a stretch-dominated deformation mechanism and the occurrence of a plastic pre-buckling stage was identified. The strength level and strain hardening potential, respectively, in this stage were controlled by the relative density of the structure, the deformation mechanisms in the steel and the steel/Mg-PSZ particle interactions.
- IP compression resulted in a lower strength and thus in a reduced energy absorption capability in comparison to OOP loading. However, altering the cell shape from square-celled to Kagome configuration contributed considerably to an enhanced IP performance.
- Decreasing the austenite stability and the stacking fault energy led to an increase of flow stress and strain hardening rate. Even though the failure strain at the peak stress decreased with decreasing nickel content, the low nickel containing samples exhibited the highest TRIP-effect, and thereby possessed the greatest energy absorption capability.
- The reinforcement with Mg-PSZ particles contributed to an increase of flow stress and energy absorption capability. Damage processes like interfacial debonding, particle cracking and crack bifurcation caused a shift of structural collapse to lower stresses and strains.

Acknowledgements This work was funded by the German Research Foundation or Deutsche Forschungsgemeinschaft (DFG), and was created as part of the Collaborative Research Center TRIP-Matrix-Composites (Project number 54473466—CRC 799). The build-up of the Freiberg Shock Wave Laboratory was fully financed by the Dr. Erich Krüger foundation. Special thanks are addressed to Dr. D. Ehinger and Dr. S. Wolf for their outstanding work in this sub-project generating numerous publications and hence significant foundation for this book chapter. Prof. T. Halle of OVGU Magdeburg supported the project with FEM-calculations. Moreover, part of the experimental work was done by Ms. C. Ullrich, Dr. M. Motylenko, Dr. A. S. Savinykh and Prof. S. V. Razorenov (RAS, Chernogolovka, Russia), for which we would like to express our sincere thanks. Additionally, the authors thank all technical employees who were tasked with mechanical processing of samples for mechanical testing and microstructure analysis as well as all students supporting the research project.

References

1. L. Remy, A. Pineau, Mater. Sci. Eng. **28**, 99 (1977)
2. O. Grässel, L. Krüger, G. Frommeyer, L.W. Meyer, Int. J. Plast **16**, 1391 (2000)
3. G. Frommeyer, U. Brüx, P. Neumann, ISIJ Int. **43**, 438 (2003)
4. O. Bouaziz, S. Allain, C. Scott, Scr. Mater. **58**, 484 (2008)
5. V.F. Zackay, E.R. Parker, D. Fahr, R. Busch, Trans. ASM **60**, 252 (1967)
6. G.B. Olson, M. Cohen, Metall. Trans. A **6**, 791 (1975)
7. I. Tamura, Met. Sci. **16**, 245 (1982)
8. S. Martin, S. Wolf, U. Martin, L. Krüger, D. Rafaja, Metall. Mater. Trans. A **47**, 49 (2016)
9. O. Bouaziz, H. Zurob, M. Huang, Steel Res. Int. **12**, 937 (2013)
10. L. Krüger, S. Decker, R. Ohser-Wiedemann, D. Ehinger, S. Martin, U. Martin, H.J. Seifert, Steel Res. Int. **82**, 1017 (2011)
11. C.G. Aneziris, W. Schärfl, H. Biermann, U. Martin, Int. J. Appl. Ceram. Technol. **6**, 727 (2009)

12. D. Ehinger, L. Krüger, S. Krause, U. Martin, C. Weigelt, C.G. Aneziris, EPJ Web Conf. **26**, 1056 (2012). https://doi.org/10.1051/epjconf/20122601056
13. A. Weiß, P.R. Scheller, A. Jahn, Patent WO 2008/009722, 24 Jan 2008
14. A. Jahn, A. Kovalev, A. Weiß, S. Wolf, L. Krüger, P.R. Scheller, Steel Res. Int. **82**, 39 (2011)
15. G.T. Gray III, Mechanical testing and evaluation, in *ASM Handbook,* vol. 8 ed. by H. Kuhn, D. Medlin (ASM International, Materials Park, OhioText, 2000), p. 462
16. D.J. Frew, Exp. Mech. **45**, 186 (2005)
17. J.C. Gong, L.E. Malvern, D.A. Jenkins, J. Eng. Mater. Technol. **112**, 309 (1990)
18. L.M. Barker, R.E. Hollenbach, J. Appl. Phys. **43**, 4669 (1972)
19. G.I. Kanel, S.V. Razorenov, V.E. Fortov (eds.), *Shock-Wave Phenomena and the Properties of Condensed Matter* (Springer, New York, 2004)
20. R. Eckner, B. Reichel, A.S. Savinykh, L. Krüger, S.V. Razorenov, G.V. Garkushin, Metall. Mater. Trans. A **47**, 75 (2016)
21. K. Thoma, U. Hornemann, M. Sauer, E. Schneider, Meteorit. Planet. Sci. **40**, 1283 (2005)
22. R. Eckner, L. Krüger, C. Ullrich, D. Rafaja, T. Schlothauer, G. Heide, Metall. Mater. Trans. A **47**, 4922 (2016)
23. S. Martin, S. Wolf, S. Decker, L. Krüger, U. Martin, Steel Res. Int. **86**, 1187 (2015)
24. A. Weidner, H. Biermann, JOM **67**, 1729 (2015)
25. L. Krüger, S. Wolf, S. Martin, U. Martin, A. Jahn, A. Weiß, P.R. Scheller, Steel Res. Int. **82**, 1087 (2011)
26. L. Krüger, S. Wolf, U. Martin, S. Martin, P.R. Scheller, A. Jahn, A. Weiß, J. Phys: Conf. Ser. **240**, 12098 (2010)
27. J. Talonen, H. Hänninen, P. Nenonen, G. Pape, Metall. Mater. Trans. A **36**, 421 (2005)
28. J. Talonen, H. Hänninen, Acta Mater. **55**, 6108 (2007)
29. M. Isakov, S. Hiermaier, V.-T. Kuokkala, Metall. Mater. Trans. A **46**, 2352 (2015)
30. T.S. Byun, Acta Mater. **51**, 3063 (2003)
31. L. Krüger, S. Wolf, M. Rüssel, U. Martin, A. Jahn, A. Weiß, P.R. Scheller, MP Materials Testing **52**, 588 (2010)
32. A. Andrade-Campos, F. Teixeira-Dias, U. Krupp, F. Barlat, E.F. Rauch, J.J. Grácio, Strain **46**, 283 (2010)
33. R. Eckner, L. Krüger, KEM **742**, 113 (2017)
34. G.L. Huang, D. Matlock, G. Krauss, Metall. Trans. A **20**, 1239 (1989)
35. A. Bäumer, J.A. Jiménez, W. Bleck, Int. J. Mater. Res. **101**, 705 (2010)
36. L. Krüger, S. Wolf, U. Martin, P. Scheller, A. Jahn, A. Weiß, in *Proceedings of the 9th International Conferences on the Mechanical and Physical Behaviour of Materials under Dynamic Loading (DYMAT 2009),* Brussels, Belgium, 7–11 September 2009
37. A.Y. Chen, H.H. Ruan, J. Wang, H.L. Chan, Q. Wang, Q. Li, J. Lu, Acta Mater. **59**, 3697 (2011)
38. S. Wolf, S. Martin, L. Krüger, U. Martin, Mater. Sci. Eng., A **594**, 72 (2014)
39. D.C. Ludwigson, J.A. Berger, J. Iron Steel Inst. **207**, 63 (1969)
40. T. Narutani, G.B. Olson, M. Cohen, J. Phys. **43**, 429 (1982)
41. S. Wolf, S. Martin, L. Krüger, U. Martin, U. Lorenz, Steel Res. Int. **83**, 529 (2012)
42. S. Wolf, Dissertation, TU Bergakademie Freiberg, 2012
43. G.R. Johnson, W.H. Cook, in *Proceedings of the 7th International Symposium on Ballistics,* The Hague, The Netherlands, 19–21 April 1983
44. S. Nemat-Nasser, Mechanical testing and evaluation, in *ASM Handbook,* vol. 8, ed. by H. Kuhn, D. Medlin (ASM International, Materials Park, OhioText, 2000), p. 429
45. L.W. Meyer, N. Herzig, T. Halle, F. Hahn, L. Krüger, K.P. Staudhammer, J. Mater. Process. Technol. **182**, 319 (2007)
46. C. Baumgart, D. Ehinger, C. Weigelt, L. Krüger, C.G. Aneziris, Compos. Struct. **136**, 297 (2016)
47. D. Borisova, V. Klemm, S. Martin, S. Wolf, D. Rafaja, Adv. Eng. Mater. **15**, 571 (2013)
48. Q. Huang, O. Volkova, H. Biermann, J. Mola, Mater. Sci. Technol. **33**, 1224 (2017)
49. D. Bancroft, E.L. Peterson, S. Minshall, J. Appl. Phys. **27**, 291 (1956)
50. L.M. Barker, R.E. Hollenbach, J. Appl. Phys. **45**, 4872 (1974)

51. S.A. Maloy, G.T. Gray, C.M. Cady, R.W. Rutherford, R.S. Hixson, Metall. Mater. Trans. A **35**, 2617 (2004)
52. L.E. Murr, J.A. Korbonski, Metall. Trans. **1**, 3333 (1970)
53. K. Chen, C. Zheng, Z. Yuan, J. Lu, X. Ren, X. Luo, Mater. Sci. Eng., A **587**, 244 (2013)
54. R. Eckner, L. Krüger, M. Motylenko, A.S. Savinykh, S.V. Razorenov, G.V. Garkushin, EPJ Web Conf. **183**, 3007 (2018). https://doi.org/10.1051/epjconf/201818303007
55. C. Ullrich, R. Eckner, L. Krüger, S. Martin, V. Klemm, D. Rafaja, Mater. Sci. Eng., A **649**, 390 (2016)
56. D. Ehinger, L. Krüger, U. Martin, C. Weigelt, C.G. Aneziris, Steel Res. Int. **82**, 1048 (2011)
57. D. Ehinger, L. Krüger, U. Martin, C. Weigelt, C.G. Aneziris, Int. J. Solids Struct. **66**, 207 (2015). https://doi.org/10.1016/j.ijsolstr.2015.02.052
58. D. Ehinger, L. Krüger, U. Martin, C. Weigelt, C.G. Aneziris, Adv. Eng. Mater. **15**, 646 (2013)
59. Q.-X. Dai, A.-D. Wang, X.-N. Cheng, X.-M. Luo, Chin. Phys. **11**, 596 (2002)
60. F. Côté, V.S. Deshpande, N.A. Fleck, A.G. Evans, Mater. Sci. Eng., A **380**, 272 (2004)
61. G.F. Bocchini, Int. J. Powder Metall **22**, 185 (1986)
62. D. Ehinger, Dissertation, TU Bergakademie Freiberg, 2013
63. L.J. Gibson, M.F. Ashby, *Cellular Solids* (Cambridge University Press, Cambridge, 1997)
64. W.E. Baker, T.C. Togami, J.C. Weydert, Int. J. Impact Eng **21**, 149 (1998)
65. U. Ballaschk, H. Berek, D. Ehinger, C.G. Aneziris, L. Krüger, Adv. Eng. Mater. **15**, 590 (2013)
66. C. Baumgart, C. Weigelt, C.G. Aneziris, L. Krüger, EPJ Web Conf. **183**, 3014 (2018). https://doi.org/10.1051/epjconf/201818303014
67. D. Ehinger, L. Krüger, U. Martin, C. Weigelt, C.G. Aneziris, Steel Res. Int. **83**, 565 (2012)
68. C. Baumgart, T. Halle, C. Weigelt, L. Krüger, C.G. Aneziris, Sci. Technol. Mater. **30**, 35 (2018)
69. V.S. Deshpande, M.F. Ashby, N.A. Fleck, Acta Mater. **49**, 1035 (2001)
70. A.-J. Wang, D.L. McDowell, J. Eng. Mater. Technol. **126**, 137 (2004)
71. M. Wendler, A. Weiß, L. Krüger, J. Mola, A. Franke, A. Kovalev, S. Wolf, Adv. Eng. Mater. **15**, 558 (2013)
72. A. Jahn, A. Kovalev, A. Weiβ, P.R. Scheller, S. Wolf, L. Krüger, S. Martin, U. Martin, in *Proceedings of the 8th European Symposium on Martensitic Transformations (ESOMAT 2009),* Prague, Czech Republic, 7–11 September 2009
73. S. Martin, S. Wolf, U. Martin, L. Krüger, Solid State Phenom. **172–174**, 172 (2011)
74. T. Iwamoto, T. Tsuta, Y. Tomita, Int. J. Mech. Sci. **40**, 173 (1998)
75. H. Schumann, Krist. Tech. **10**, 401 (1975)
76. A. Jahn, A. Kovalev, A. Weiß, P.R. Scheller, Steel Res. Int. **82**, 1108 (2011)
77. S. Martin, C. Ullrich, D. Šimek, U. Martin, D. Rafaja, J. Appl. Crystallogr. **44**, 779 (2011)
78. G.B. Olson, M. Cohen, Metall. Trans. A **7**, 1897 (1976)
79. F. Lecroisey, A. Pineau, Metall. Mater. Trans. B **3**, 391 (1972)
80. N. Chawla, Y.-L. Shen, Adv. Eng. Mater. **3**, 357 (2001)
81. S. Martin, S. Richter, S. Decker, U. Martin, L. Krüger, D. Rafaja, Steel Res. Int. **82**, 1133 (2011)
82. H. Berek, A. Yanina, C. Weigelt, C.G. Aneziris, Steel Res. Int. **82**, 1094 (2011)
83. C. Weigelt, S. Giersberg, C. Wenzel, C.G. Aneziris, Adv. Eng. Mater. **12**, 486 (2010)
84. C. Weigelt, C.G. Aneziris, H. Berek, D. Ehinger, U. Martin, Adv. Eng. Mater. **14**, 53 (2012)